



# Inducing electronic asymmetry on Ru clusters to boost key reaction steps in basic hydrogen evolution

Jin-Tao Ren<sup>a</sup>, Lei Chen<sup>a</sup>, Hao-Yu Wang<sup>a</sup>, Wen-Wen Tian<sup>a</sup>, Xu Zhang<sup>b,\*</sup>, Tian-Yi Ma<sup>c,\*</sup>, Zhen Zhou<sup>a</sup>, Zhong-Yong Yuan<sup>a,\*</sup>

<sup>a</sup> Key Laboratory of Advanced Energy Materials Chemistry (Ministry of Education), School of Materials Science and Engineering, Smart Sensing Interdisciplinary Science Center, Nankai University, Tianjin 300350, China

<sup>b</sup> School of Chemical Engineering, Zhengzhou University, Zhengzhou 450001, China

<sup>c</sup> School of Science, RMIT University, Melbourne, VIC 3000, Australia

## ARTICLE INFO

### Keywords:

Electronic asymmetry  
Ruthenium  
Interfacial interaction  
Hydrogen evolution reaction

## ABSTRACT

Modulating electronic asymmetry of catalysts is a novel option to regulate the electrocatalytic performance. Nevertheless, the efficient regulation of asymmetric degree of heterostructured catalysts at the atomic level still remains challenging. Herein, Ru nanoclusters (NCs, average particle size of  $\sim 1.3$  nm) were anchored on carbon materials doped by controllable N functional groups to optimize the electronic asymmetry toward efficient hydrogen evolution reaction (HER). The electronic interaction between Ru and N species, and hence, the asymmetric electronic distribution of Ru NCs is subjectively manipulated by precisely tailoring the type of N dopants, especially pyrrolic-N, of carbon substrates. As a result, the pyrrolic-N dominated Ru-based heterostructures exhibit excellent HER activity compared to most of the current Ru-based electrocatalysts in basic media. Multiple spectroscopy experiments and density functional theory simulations demonstrate that the asymmetric distribution of surface electron of Ru-based heterostructures not only accelerates  $H_2O$  adsorption and dissociation at interfacial Ru sites with positive charge but also facilitates the adsorption behavior of hydrogen on surface Ru sites with negative charge, thereby simultaneously optimizing the elementary steps in basic HER process. The present findings would provide some crucial understanding in manipulating the local electronic asymmetry toward reasonable design and fabrication of advanced catalysts and beyond.

## 1. Introduction

Hydrogen evolution reaction (HER) has been considered as a promising approach to achieve sustainable energy-to-hydrogen production [1,2]. However, the polarization phenomenon occurring at electrode induces the large overpotential, which requires the highly efficient catalysts to accelerate the sluggish apparent reaction kinetics [3,4]. To date, various strategies such as interface coupling, alloying, strain engineering have been proposed to regulate the electronic structure of metal-based HER catalysts for boosting the electrocatalytic performance [5,6]. In addition, with respect to metal-free carbon materials, heteroatoms doping is one of the most effective approaches to control the charge distribution of carbon framework and engineer highly active centers of HER [7,8]. Undoubtedly, the specific electronic environment of active centers induced by charge redistribution can be obtained by irregularly distorting periodic structure, thereby significantly boosting

the electrocatalytic activity. However, the existing research justly focuses on the adjustment of the charge distribution of active centers by engineering advanced structures, while the degrees of asymmetry is scarcely considered. Besides, in order to subjectively control electronic distribution of catalysts to improve electrocatalytic activity, the design of asymmetric structure with regular charge distribution beyond the irregular structure will be more efficient [9,10]. In fact, the regular asymmetry engineering, for instance, piezoelectric polarization and ferroelectric polarization, has been regarded as an efficient strategy to accelerate photogenerated charge separation of photocatalysts to improve activity, while it is scarcely implemented in electrocatalytic fields [11,12].

Generally, the reaction rate of catalysts toward HER in basic condition is about 2–3 orders of magnitude lower than that in acidic electrolyte due to the larger activation energy used for  $H_2O$  dissociation to supply required  $H^+$  [13,14]. Thus, developing highly efficient

\* Corresponding authors.

E-mail addresses: [zzuzhangxu@zzu.edu.cn](mailto:zzuzhangxu@zzu.edu.cn) (X. Zhang), [tianyi.ma@rmit.edu.au](mailto:tianyi.ma@rmit.edu.au) (T.-Y. Ma), [zyyuan@nankai.edu.cn](mailto:zyyuan@nankai.edu.cn) (Z.-Y. Yuan).

<https://doi.org/10.1016/j.apcatb.2023.122466>

Received 23 December 2022; Received in revised form 17 January 2023; Accepted 11 February 2023

Available online 13 February 2023

0926-3373/© 2023 Elsevier B.V. All rights reserved.

electrocatalysts to achieve high performance in basic electrolyte is pressing but still challenging. Ruthenium (Ru) has been considered as a potential substitute for the state-of-the-art platinum (Pt)-based electrocatalysts for HER by virtue of the cheap price and great water adsorption/dissociation ability [15,16]. Nevertheless, the high bonding strength of Ru to  $H^*$  / $OH^*$  intermediates significantly hampers the further improved HER activity [17,18]. Some recent studies have manifested that modulating surface electronic environment of Ru-based catalysts by heterointerface construction is an effective strategy to optimize bonding strength of  $H^*$  / $OH^*$  in basic HER. For instance, Song et al. [19] demonstrated that the Ru single atoms and adjacent Ru nanoparticles synergistically promote each other to transfer electron to carbon substrates, which accelerate water dissociation and reduce energy barrier of  $H^*$  / $OH^*$  desorption on adjacent Ru sites, eventually, optimize the reaction kinetics of the developed Ru-based catalysts in basic media. Subsequently, some transition metals and their derivatives with Ru were also employed to construct heterostructure catalysts (e.g. Mo-Ru NSAs [20] and Ru/P-TiO<sub>2</sub> [21]) to optimize the electronic structure of Ru to achieve the appropriate bonding strength of key intermediates. Despite such heterointerface strategy is a valid approach to regulate the electron distribution of Ru-based electrocatalysts, it is difficult to precisely and simultaneously control the asymmetry strength, accurate structure, and amount of Ru active sites for high basic HER performance [22]. Therefore, in view of regulating electronic distribution to achieve highly electrocatalytic efficiency and deepening the mechanistic understanding, the advanced Ru-based catalysts should be precisely designed and fabricated to achieve a regular electronic asymmetry of Ru nanoparticles at molecular level.

Herein, we report the asymmetry tactic for designing Ru-based catalysts to accurately control the electronic asymmetry of active species and their basic HER electrocatalytic activity for the first time. To implement this purpose, the defect carbon with adjustable N functional groups was fabricated, which was employed as carbon substrate to regulate the electronic asymmetry of the supported Ru nanoclusters (NCs). X-ray photoelectron spectroscopy and Kelvin probe atomic force microscopy verify the significant asymmetric electronic distribution on Ru NCs induced by the pyrrolic-N compared to other type of N functional groups. In detail, the pyrrolic-N dominated carbon supported Ru NCs exhibits a remarkable HER performance in 1.0 M KOH, delivering the small overpotential of 28.5 mV at 10 mA cm<sup>-2</sup>, Tafel slope of 20.8 mV dec<sup>-1</sup>, large mass activity of 4.02 A mg<sup>-1</sup> (100 mV), and turnover frequency of 13.5 H<sub>2</sub> s<sup>-1</sup> (50 mV), superior to most of reported Ru-based catalysts and commercial Pt/C catalyst. This Ru-based catalyst also exhibits excellent single-cell performance for anion exchange membrane water electrolysis. Density functional theory (DFT) calculation proves the unique function of pyrrolic-N in regulating the surface electronic asymmetry degree of anchored Ru NCs, thereby creating different active sites on Ru NCs to meet different requirements of multiple reaction steps in basic HER process.

## 2. Experimental section

### 2.1. Preparation of N-doped defect carbon (NDC)

Typically, a mixture of 50 mg DC, and 200 mg mixture of melamine and glycine with a mass ratio of 16:0, 1:1, 4:1, 8:1, and 12:1 were added into 40 mL deionized water under stirring for 5 h in room temperature. Then the mixed solution was stirred and heated at 80 °C to evaporate the water. The dried sample was ground in a mortar and placed in a tube furnace under an Ar atmosphere (heating rate of 5 °C min<sup>-1</sup>) at 350 °C for 3 h, followed by pyrolysis at 800 °C for 1 h. And the resultant samples were labeled as NDC-x (x represents 0, 1, 4, 8, 12).

### 2.2. Synthesis of N-doped defect carbon with Ru nanoclusters (Ru/NDC)

To prepare Ru/NDC samples, 50 mg of the as-prepared NDC-x and

480 μL of 0.1 M ruthenium (III) chloride hydrate (RuCl<sub>3</sub>•3 H<sub>2</sub>O) aqueous solution were added into the mixed solution containing 10 mL of deionized water and 30 mL of ethanol under vigorous magnetic stirring. Finally, the mixed solution was stirred and heated at 80 °C. The resultant solid samples were annealed at 400 °C for 2 h under 5%H<sub>2</sub>/Ar atmosphere. The resultant catalyst powder was obtained after slowly cooling to room temperature. The metal Ru content of the resultant sample was measured by TGA analysis. And the prepared samples were labeled as Ru/NDC-x (x represents 0, 1, 4, 8, 12). To optimal the mass loading of Ru on NDC, a series of Ru-y/NDC-4 (y represents the Ru loading) with different Ru loading on NDC-4 were prepared. Specially, 50 mg of the as-prepared NDC-4 and the different amount of 0.1 M RuCl<sub>3</sub>•3 H<sub>2</sub>O aqueous solution (120, 240, 480, 720, and 1000 μL) were added into the mixed solution containing 10 mL of deionized water and 30 mL of ethanol under vigorous magnetic stirring. After that, the resultant sample was treated by the identical procedures to that of Ru/NDC-x. And the resultant samples were named as Ru-y/NDC-4 (y represents Ru loading).

### 2.3. Preparation of defect carbon supported Ru nanoparticles (Ru/DC)

The Ru/DC was prepared by the same method to Ru/NDC-x expect for the NDC-x was replaced by DC. The metal Ru content of the resultant sample was measured by TGA.

Other details of materials characterization and electrochemical measurements were provided in Supporting Information (SI).

## 3. Results and discussion

The Ru NCs loaded on N-doped defect carbon (NDC) were designed and synthesized via the impregnation method and subsequent pyrolysis, as illustrated in Fig. 1a. Specially, the ratio of N functional groups of NDC is subjectively controlled by changing the mass ratio of melamine and glycine. Suffering from the carbonization stage, the N-enriched melamine was converted to pyridinic-N and graphitic-N, while the dehydration effect of glycine would facilitate the conversion of pyridinic-N to pyrrolic-N [23]. Compared with pristine defect carbon (DC), the Raman spectrum (Fig. S1) of NDC-4 exhibits a larger intensity ratio of D and G bands ( $I_D/I_G$ ), indicating that the N doping induces more defects [24]. Low-resolution TEM images of Ru/NDC-x (Figs. 1b, S3) exhibit that Ru NCs with the loosely packed dispersion are homogeneously anchored on the NDC substrates. With respect to Ru/NDC-x catalysts under further magnification (Fig. 1c, S4), the average particle size of Ru NCs is about 1.3 nm, which is lower than that of Ru/DC catalyst (~3.3 nm) (Fig. S5). Specially, the Ru NCs in Ru/NDC-4 (Fig. 1d) are well crystallized and presented by (101) crystal plane. The fast Fourier transform (FFT) pattern (Fig. 1e) displays the hexagonal close-packed (hcp) lattice of the selected Ru NCs. And the selected area electron diffraction (SAED) pattern of Ru/NDC-4 (Fig. 1f) only exhibits the typical diffraction rings ascribed to graphitic carbon, which should be ascribed to the ultrafine particle diameter of those dispersed Ru NCs on carbon substrates. Scanning TEM (Fig. 1g) and HAADF-STEM (Fig. 1h) images further exhibit the uniformly distributed Ru NCs on NDC. STEM-EDX mapping of Ru/NDC-4 (Fig. 1i-k) reveals the successful doping of N in carbon frameworks, and the Ru element aggregated NCs are also dispersed over carbon substrates.

As seen from the powder XRD patterns of Ru/NDC-4 with different Ru loading (Fig. 2a), when the Ru loading is below 4.37 wt%, there only exhibits the broad diffraction peak at around 26° (2θ), ascribing to the carbon (002) peak, which is caused by the lower loading and the ultra-small dimension of the formed Ru NCs on NDC. The Ru content on NDC was determined by TGA analysis (Fig. S6). Further increasing Ru loading to 8.02 wt%, the new diffraction peak at about 44° (2θ) can be indexed to the (101) crystal facet of metallic Ru phase (PDF # 65-7646). Furthermore, a series of well-defined peaks coincident with (100), (002), (101), (102), (110), and (103) planes of Ru NCs are observed on

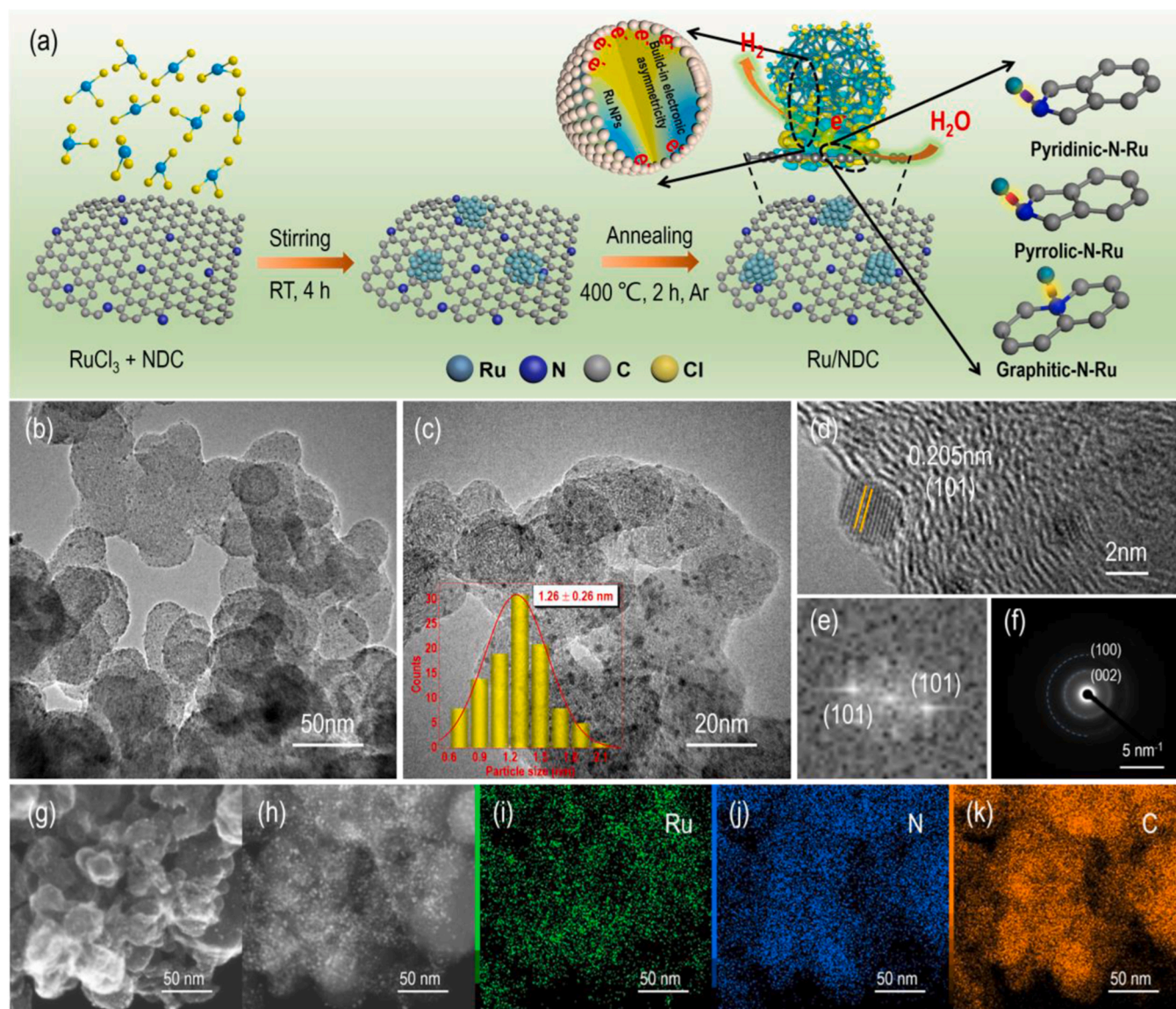


**Fig. 1.** (a) The synthetic route for Ru/NDC with electronic asymmetry. (b,c) TEM images of Ru/NDC-4. Inset in (c): the corresponding Ru particle size distribution histogram. (d) High-resolution TEM image of Ru/NDC-4. (e) The FFT pattern of a selected Ru NCs in (d). (f) SAED pattern of Ru/NDC-4. (g) Scanning TEM image, (h) high-angle annular dark-field (HAADF)-STEM, and corresponding STEM-energy-dispersive X-ray spectroscopy (STEM-EDX) mapping of Ru (i), N (j), and C (k) of Ru/NDC-4.

Ru/NDC-4 with a higher Ru loading of 17.05 wt%. In addition, the XRD patterns of Ru/NDC-*x* (Fig. S7) exhibit the similar diffraction peaks with monotonous features, demonstrating their identical crystalline structure under the same fabrication process. The content of Ru in Ru/NDC-*x* is calculated to be about 8 wt%, as measured by TGA (Fig. S8), which is consistent with the results of ICP-OES. It should be noted that the Ru loading in Ru/NDC-*x* is higher than that of Ru/DC (7.19 wt%) under the identical preparation conditions, while the Ru/DC exhibits relatively higher diffraction intensity at 44° (2θ), manifesting the positive effect of N doping to tether Ru atoms during the pyrolysis process, thereby improving the mass loading and particle dispersion. The prepared Ru/NDC-*x* have almost identical N<sub>2</sub> sorption isotherms and Brunauer-Emmett-Teller (BET) surface areas (Fig. S9), manifesting that adjusting N functional group ratio has negligible influence on the textural structure of catalysts.

The difference of surface charge states and electronic structures of Ru/NDC-*x* with different N ratios was investigated by XPS. XPS full spectra (Fig. S10) manifest the existence of the target elements of C, N, Ru, and O with the nearly identical element contents. With respect to C

1 s spectra (Fig. S11a), all Ru/NDC-*x* samples exhibit four fitted signals, ascribing to the graphitized *sp*<sup>2</sup> carbon (C=C) (284.8 eV), C–N(O) (286.0 eV), C=N(O) (287.5 eV), and –COOH (289.0 eV), respectively [25,26]. As for Ru 3d<sub>5/2</sub> spectra (Fig. S11b), the former fitted peak can be attributed to metallic Ru<sup>0</sup>, the latter and its satellite peak correspond to the oxidized Ru components (Ru<sup>x+</sup>) [27]. And the similar situation is also observed in the Ru 3d<sub>3/2</sub> region. Notably, it can be detected from Ru 3d<sub>5/2</sub> spectra that the Ru<sup>0</sup> 3d<sub>5/2</sub> peak shifts negatively from Ru/NDC-4 to Ru/NDC-0, especially to Ru/DC, indicating the electron donation process of Ru NCs associated with the electronic change of the carbon substrates.

The N 1 s spectra (Fig. 2b) of Ru/NDC-4 can be fitted to pyridinic-N (398.7 eV), pyrrolic-N (400.0 eV), graphitic-N (401.2 eV), and oxidized-N (403.7 eV), respectively [28,29]. As shown on the magnified observations (Fig. S12b), concomitantly, the binding energy of pyrrolic-N in N 1 s for Ru/NDC-4 is negatively shifted of 0.16 eV in comparison with Ru-free NDC-4, whilst the shift in the binding energy of pyridinic-N or graphitic-N is indistinctive. The difference of N 1 s spectra demonstrates that Ru NCs tend to bind with N-doped DC primarily *via* pyrrolic-N. The



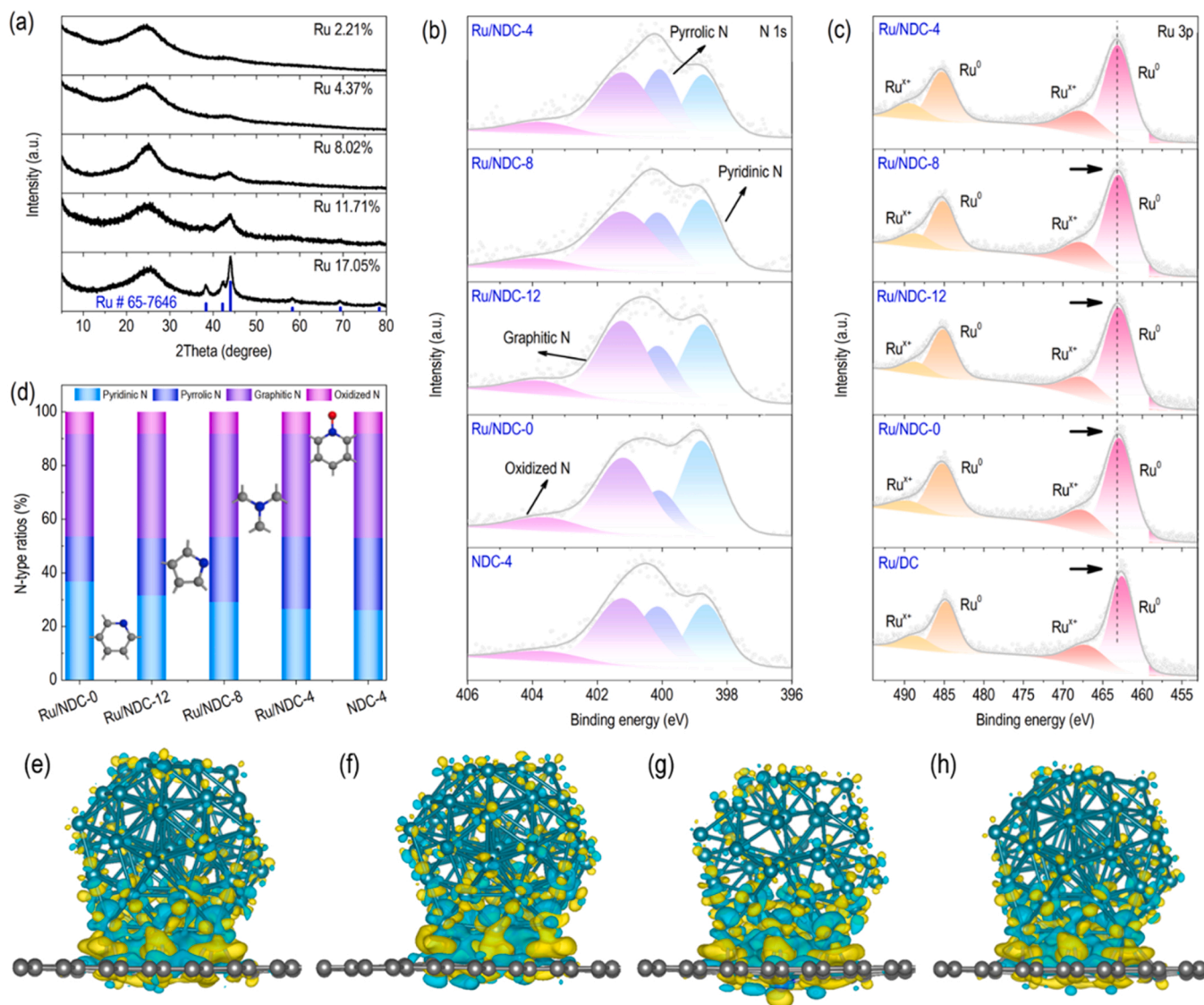


**Fig. 2.** (a) XRD pattern of Ru/NDC-4 with different mass loading of Ru. (b) High-resolution XPS spectra of N 1s for Ru/NDC-x and NDC-4. (c) High-resolution XPS spectra of Ru 3p for Ru/NDC-x and Ru/DC. (d) Ratios for different N configurations of Ru/NDC-x and NDC-4. 3D charge density differences of Ru<sub>55</sub> clusters loaded graphene with pyridinic-N (e), graphene with pyrrolic-N (f), graphene with graphitic-N (g), and graphene without N doping (h) with an isosurface of 0.002 e Å<sup>-3</sup>. The yellow and cyan regions represent the accumulation and depletion of the electron, respectively.

low availability of long pair of electron in pyrrolic-N (as it exists in conjugation system) endows it with high electronegativity [30,31]. Therefore, pyrrolic-N possesses the capability to withdraw electron density from Ru in comparison with pyridinic-N or graphitic-N, thus inducing the downshift of d-band center of Ru [32,33]. From those N 1s spectra of Ru/NDC-x (Fig. 2b) and the ratio of N functional groups on Ru/NDC-x (Fig. 2d), it can be found that the mass ratio of melamine and glycine exerts significant influence on the proportion of N functional groups in Ru/NDC-x. The proportion of pyridinic-N in Ru/NDC-x decreases as the increase of glycine, whilst the proportion of pyrrolic-N exhibits the reverse trend, and the proportion of graphitic-N and oxidized-N have slight fluctuation. Impressively, Ru/NDC-4 exhibits the largest proportion of pyrrolic-N among all Ru/NDC-x, which is beneficial to coordinate with more Ru atoms and strengthen the interaction between Ru NCs and NDC at heterointerfaces, thereby manipulating the electrocatalytic activity and the structural stability of Ru/NDC-4 during electrocatalysis [34].

In the Ru 3p spectra (Fig. 2c) of Ru/NDC-x, a pair of significant peaks are ascribed to Ru 3p<sub>3/2</sub> and Ru 3p<sub>1/2</sub> of Ru<sup>0</sup>, respectively [35,36]. The attendant weak signals can be attributed to Ru<sup>x+</sup>, owing to exposure to

air [37]. Consistent with the observation in Ru 3d, the binding energy of Ru<sup>0</sup> also exhibits the negative shift from Ru/NDC-4 to Ru/NDC-0, demonstrating the different electronic configuration of Ru NCs in those Ru/NDC-x. Specially, compared to N-free Ru/DC, there is 0.55 eV positive shift of Ru<sup>0</sup> for Ru/NDC-4 in Ru 3p spectra, which means that N-doped DC changes the electronic configuration of the anchored Ru NCs, and a transfer of Ru d-electron to N-doped DC. More importantly, the magnified observations in Fig. S11c exhibit that the shifted binding energies of Ru 3p in those Ru/NDC-x are different, indicating that the microenvironment of carbon substrates has the direct impact on the electron distribution over Ru NCs, wherein the shifted binding energy of Ru 3p in Ru/NDC-4 (the highest pyrrolic-N content) is largest. Meanwhile, from the Raman spectra in Fig. S13, compared to NDC-4, the G band of Ru/NDC-4 exhibits an evident blue shift about 6 cm<sup>-1</sup>. It further manifests that there exists a significant interface electronic interaction between Ru NCs and NDC and electrons transfer from Ru NCs to NDC substrates [38,39].

The electronic characteristics including the deformation charge density and Bader charge analysis were simulated to further understand the electronic interaction between Ru NCs and NDC substrates as well as



the surface electron distribution on Ru NCs. As model systems (Fig. S14), Ru<sub>55</sub> clusters were used for the Ru NCs, and Ru<sub>55</sub> placed in the N-doped graphene was used for Ru/NDC. The atom number of Ru clusters was set at 55, which is identical to about 1.2 nm diameter because the TEM analysis indicates the 1.27 nm average nanoparticle diameter of the developed Ru NCs. Represented by the extended scale of both electron accumulation and depletion regions on the Ru<sub>55</sub> clusters (Fig. 2e-h), the surface electrons are inclined to redistribute and accumulate around the Ru-carbon interfaces. The delocalization of electrons induces the redistribution of charges on the supported Ru NCs, leading to the variation of the localized electron distribution asymmetry degree. Bader charge numbers of Ru<sub>55</sub> clusters were further calculated, and this charge numbers can be employed as the descriptor to quantify the asymmetry degree of Ru<sub>55</sub> clusters. The type of N functional groups has an evident impact on the electron interaction between Ru<sub>55</sub> cluster and graphene, wherein the pyrrolic-N doped graphene obtains more electrons from Ru<sub>55</sub> (1.72 e<sup>-</sup>) than that of pyridinic-N (1.50 e<sup>-</sup>) and graphitic-N (1.38 e<sup>-</sup>), as well as N-free graphene (1.28 e<sup>-</sup>). Therefore, all these proofs demonstrate that the interfacial Ru sites are positively charged resulting from the loss of electron, while the surface Ru atoms are relatively electron-enriched compared to the interfacial ones, thus subjectively constructing regular asymmetric structure with regular electronic distribution.

For the purpose of evaluating the significance of the electronic asymmetry for electrocatalysis, the HER performances of Ru/NDC-x were measured in H<sub>2</sub>-saturated 1.0 M KOH. Prior to electrochemical measurements, the Ru loading on NDC was firstly optimized. Determined from their polarization curves in Fig. S16, the Ru loading of 8.02 wt% acquires the highest HER activity. Therefore, all the following discussed catalysts were prepared under this condition to ensure the optimal mass loading of Ru species. The HER activity of Ru/NDC-x was

examined after being loaded on glassy carbon electrode (diameter = 5.0 mm, catalyst loading: 0.384 mg cm<sup>-2</sup>, equals to Ru loading of ~30.8 μg cm<sup>-2</sup>). As shown in Fig. 3a, Ru/DC exhibits the low HER performance with the overpotential of 59.2 mV at -10 mA cm<sup>-2</sup>. After the introduction of N dopant, HER performances of Ru/NDC-x are progressively improved (Fig. S17). Unexpectedly, Ru/NDC-4 displays the best HER activity with a smallest overpotential of 28.5 mV at -10 mA cm<sup>-2</sup>, which is lower than that of commercial 20% Pt/C catalyst (31.9 mV) even though the Ru loading is much lower than Pt loading (30.8 vs. 71.5 μg cm<sup>-2</sup>). According to the Tafel plots derived from their polarization curves (Fig. 3b), Ru/NDC-4 exhibits a Tafel slope of 20.8 mV dec<sup>-1</sup>, which is smaller than 20% Pt/C (27.6 mV dec<sup>-1</sup>), Ru/DC (67.1 mV dec<sup>-1</sup>), and other Ru/NDC-x (Fig. S18), indicating that the HER pathway of Ru/NDC-4 follows Volmer-Tafel mechanism [40,41].

To exclude the impact of Ru loading on each catalyst toward HER activity, the mass activity of Ru/NDC-x was further determined. As displayed in Fig. 3c, Ru/NDC-4 still exhibits much higher mass activity than other samples under the same conditions, for instance, it obtains a mass activity of 4.02 A mg<sub>Ru</sub><sup>-1</sup> at overpotential of 100 mV. To reflect the intrinsic HER activities, the electrocatalytically active surface area (ECSA) of electrocatalysts were measured by employing the copper underpotential deposition (Cu-UPD) method (Fig. S19) [25,42]. Based on ECSA, the turnover frequency (TOF) as function of potentials was obtained (Fig. 3d). Specially, Ru/NDC-4 presents a TOF of 13.5 s<sup>-1</sup> at overpotential of 50 mV, which is superior to those of 20% Pt/C and other Ru/NDC-x. Exchange current density (*J*<sub>0</sub>) is another key descriptor that provides intrinsic ability of charge transfer among catalyst surface and electrolyte, which can be determined by fitting kinetic current density into the Butler-Volmer equation at the micropolarization region (-20 - 20 mV vs. RHE) [43]. The *J*<sub>0</sub> for Ru/NDC-4 is 2.52 mA cm<sup>-2</sup>, which is higher than that of 20% Pt/C and other Ru/NDC-x samples

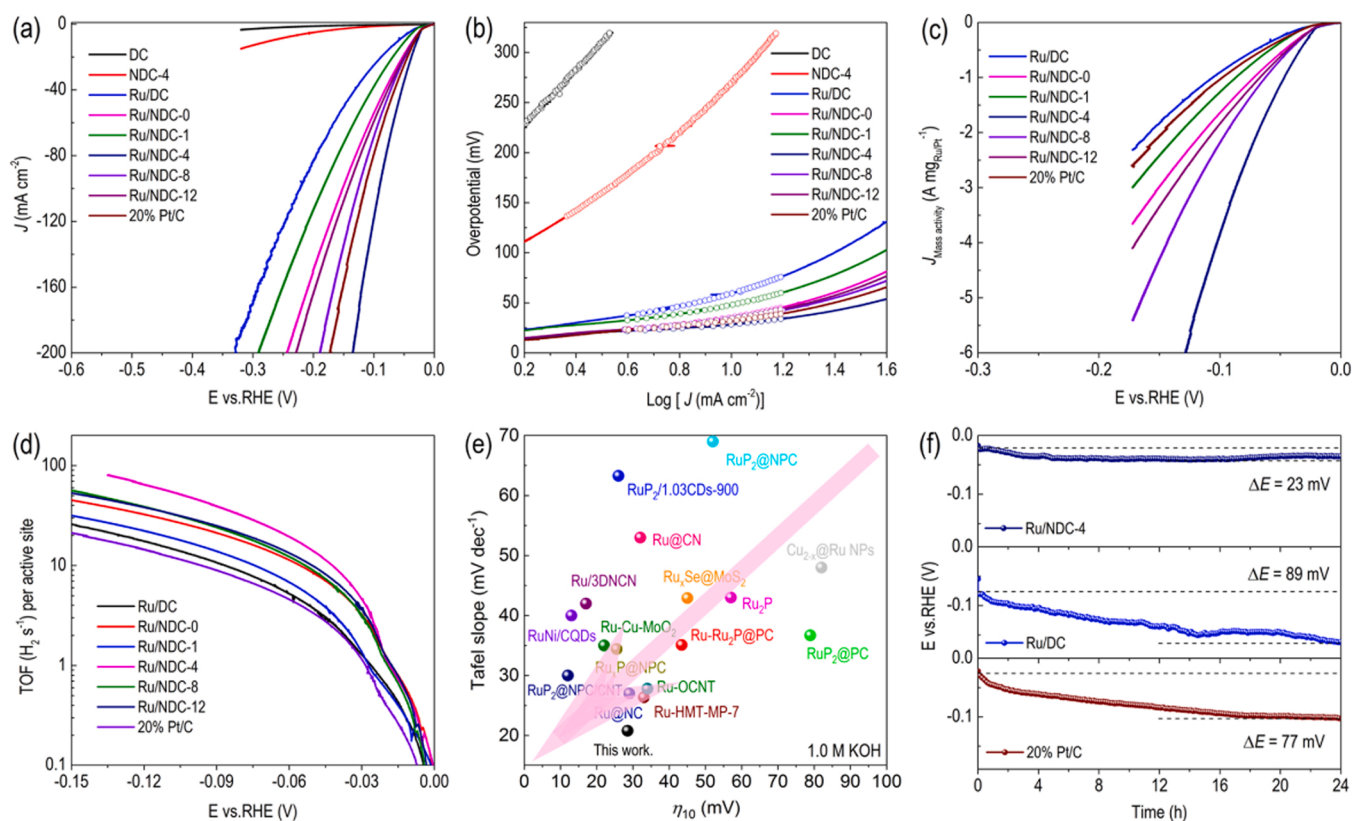


**Fig. 3.** Electrochemical measurements of HER in H<sub>2</sub>-saturated 1.0 M KOH. (a) LSV polarization curves of the developed catalysts. (b) Tafel plots obtained from LSV curves. (c) Mass activities of the developed catalysts and 20% Pt/C. (d) Relationship between TOF values and the potentials of the developed catalysts and 20% Pt/C. (e) Comparison of overpotentials at -10 mA cm<sup>-2</sup> and Tafel slope between Ru/NDC-4 and recently reported Ru-based electrocatalysts in 1.0 M KOH. (f) Potential-time stability curves of Ru/NDC-4, Ru/DC, and 20% Pt/C catalyst under the current density of -10 mA cm<sup>-2</sup>.

(Fig. S20). The electron transfer ability of those fabricated electrocatalysts was investigated by electrochemical impedance spectroscopy (EIS). As displayed in Nyquist plots (Fig. S21), the smaller charge transfer resistance ( $R_{ct}$ ) of Ru/NDC-4 compared to other samples implies the improved interfacial electron transport capacity and the rapid reaction kinetics [44,45]. Such impressive HER performance of Ru/NDC-4 is far superior to many existing Ru-based catalysts in alkaline media, as listed in Fig. 3e and Table S2, demonstrating the significant potential of Ru/NDC-4 to replace noble metal Pt/C benchmark for practical applications.

Besides great activity, the long-term durability is another critical criterion in electrocatalyst evaluation. Ru/NDC-4 presents little degradation with an increase in overpotential of only 23 mV after chronopotentiometry (CP) measurement at  $-10 \text{ mA cm}^{-2}$  within 24 h (Fig. 3f). However, Ru/DC exhibits the severe potential increment (89 mV) and 20% Pt/C catalyst also shows a large overpotential loss (77 mV) under the same conditions. The additional characterizations were conducted to investigate the superior stability of Ru/NDC-4. As shown in the TEM images (Fig. S22), Ru NCs on the used Ru/NDC-4 maintain initial morphology and structure without evident agglomeration, while the average particles diameter of Ru NCs on the used Ru/DC increases from the initial 3.3–4.2 nm (Fig. S23). Moreover, the EDX mapping of the used Ru/NDC-4 (Fig. S24) exhibits the homogeneous element distribution. Meanwhile, the used Ru/NDC-4 exhibits little difference in Ru content compared to the initial catalyst (7.93 wt% vs. 8.05 wt%) on the basis of ICP analysis. The XRD pattern (Fig. S25) of the used Ru/NDC-4 exhibits the characteristic peaks similar to its initial observation. The XPS was carried out to track the chemical states of Ru NCs after stability test. The Ru NCs still maintain a near zero-valent state after HER (Fig. S26). Actually, the calculated binding energy between  $\text{Ru}_{55}$  cluster and pyrrolic-N doped graphene is  $-9.53 \text{ eV}$ , which is more negative than that of pyridinic-N doped graphene ( $-6.96 \text{ eV}$ ), graphitic-N doped graphene ( $-6.23 \text{ eV}$ ), and N-free graphene ( $-5.72 \text{ eV}$ ), verifying the strong electronic interaction between Ru NCs and pyrrolic-N dominated carbon substrates, thus contributing to the robust stability [46,47]. Moreover, this Ru/NDC-4 still exhibits excellent durability within 33 h on the multistep chronoamperometry (Fig. S27) at larger current densities, highlighting the potential for practical  $\text{H}_2$  production. Moreover, with the assistance of the water-gas displacing method (Fig. S28), the Faradaic efficiency of the Ru/NDC-4-catalyzed HER process is approaching 100%, indicating that nearly all the electrons are involved in the electrocatalytic reactions.

To reflect the universality of the prepared electrocatalysts, the HER performance was also investigated in acidic electrolyte (0.5 M  $\text{H}_2\text{SO}_4$ ). As seen in Fig. S29a, it can be observed that the acidic HER activity of the Ru/NDC-x exhibits the identical trend to that in alkaline media. The designed Ru/NDC-4 still exhibits the highest activity with the smallest overpotential of 18.8 mV to afford  $-10 \text{ mA cm}^{-2}$  in comparison with other Ru/NDC-x samples. Moreover, this Ru/NDC-4 presents the lower Tafel slope of  $27.9 \text{ mV dec}^{-1}$  relative to the other samples (Fig. S29b), which is consistent with its lower charge transfer resistance (Fig. S29c), verifying the faster reaction kinetics toward HER. No obvious decay, as proved by the chronopotentiometry test (Fig. S29d), is observed after continuous stability testing. The HER performance of Ru/NDC-x was further explored in free proton-lacked neutral electrolyte. As shown in Fig. S30a, the as-prepared Ru/NDC-4 catalyst also exhibits the best activity compared with other Ru/NDC-x catalysts, presenting smallest overpotential of 148.7 mV at  $-10 \text{ mA cm}^{-2}$  in 1.0 M buffer solution. And the larger current density ( $-100 \text{ mA cm}^{-2}$ ) of Ru/NDC-4 just requires the overpotential of 394.7 mV, which is superior to that of 20% Pt/C catalyst (429.1 mV). The Tafel slope of Ru/NDC-4 (Fig. S30b) is lower than that of other Ru/NDC-x samples and Ru/DC, meaning the favorable reaction kinetics of Ru/NDC-4 for  $\text{H}_2\text{O}$  adsorption and dissociation, which is consistent with their EIS results (Fig. S30c). Chronopotentiometry measurement (Fig. S30d) confirms the long-term electrocatalytic durability of Ru/NDC-4. Overall, the above

experimental measurements persuasively demonstrate that the Ru/NDC-4 with strong interface interaction structure is highly active and stable for HER electrolysis under the various pH regions.

To demonstrate the practical feasibility, the anion exchange membrane water electrolysis (AEMWE) tests were investigated by using the developed Ru/NDC as the cathode catalyst and the commercial  $\text{IrO}_2$  as the anode catalyst. Usually, AEMWE is operated at a relatively safe and non-corrosive alkaline conditions and integrates the advantages of both alkaline liquid electrolyte- and proton-exchange-membrane-based water electrolysis devices [48]. Therefore, AEMWE is recognized as a promising technology to satisfy the cost-effective option of  $\text{H}_2$  production. The illustration of AEMWE with the membrane electrode assembly is shown in Fig. 4a. Fig. 4b exhibits the polarization curves of the assembled AEMWE cell with Ru/NDC-4, Ru/DC, or 20% Pt/C as cathode catalyst. Obviously, Ru/NDC-4 formed AEMWE delivers the higher cell performance with the current density of  $0.72 \text{ A cm}^{-2}$  at 2.0 V, superior to that of Ru/DC- or 20% Pt/C-based cell under the same working conditions. EIS measurement performed at 1.60 V reveals that the improved cell performance of Ru/NDC-4 should be mostly ascribed to the decreased charge transfer resistance with the lowest semicircle in Nyquist plots (Fig. S31). In addition, Ru/NDC-4-based cell also displays a reliable stability at high current density of  $0.28 \text{ A cm}^{-2}$  of up to 12 h with 95.3% activity retention (Fig. 4c).

From the electrocatalytic measurements, it is clearly presented that the type of N functional groups has a decisive influence on Ru/NDC-x toward HER. To further identify the function of the electronic effect of different N types and Ru NCs on HER activity, the control samples of Ru/NDC-x with the larger proportion of single N type were prepared. The TEM images (Figs. S3, S4) and XPS spectra (Fig. S32) verify the successful fabrication of Ru/NDC-0 (highest pyridinic-N ratio of 36.82%) and Ru/NDC-1 (highest pyrrolic-N ratio of 30.07%). Despite they have the similar N content, Ru/NDC-0 exhibits the inferior HER activity in comparison with Ru/NDC-4 (Fig. 3a). In addition, Ru/NDC-4 presents better HER activity than Ru/NDC-1, which may be due to the lower N content of Ru/NDC-1 (1.83 at%) compared to Ru/NDC-4 (3.52 at%). All results again indicate that the HER activity of Ru/NDC-x should be significantly determined by the ratio of pyrrolic-N as well as its content, of course, the interaction between pyridinic-N/graphitic-N and Ru NCs also contributions to HER activity. To further understand the correlation between the content of different N functional groups and HER activity, the relationship between HER parameters (e.g. overpotential at  $-10 \text{ mA cm}^{-2}$ , Tafel slope, and  $J_0$ ) and the content ratio of N functional groups for Ru/NDC-x ( $x = 4, 8, 12, 0$ ) were established. As plotted in Fig. 4d-f, the HER performance exhibits a positive linear dependence to the content of pyrrolic-N, rather than pyridinic-N or graphitic-N, demonstrating that the larger content of pyrrolic-N is, the greater the intrinsic HER activities for Ru/NDC-x will be.

To further investigate the interface induced asymmetrical electronic distribution of Ru NCs on HER activity, the surface charges of Ru/NDC-x ( $x = 4, 8, 12$ ) and Ru/DC were carefully explored by employing Kelvin probe force microscopy (Figs. S33, 4g). As shown in Fig. 4h, the potential profiles of samples coincide with their electrocatalytic performance. N-free Ru/DC exhibits a potential difference of only 86.1 mV, indicating the weakening surface polarization of Ru NCs. While the potential difference of Ru/NDC-4 increases to 146.3 mV, which results from the improved charge interaction between Ru NCs and N-doped DC substrates. In addition, along with the decrease of pyrrolic N content, the potential is also progressively decreased, as proved by the potential difference order of  $\text{Ru/NDC-4} > \text{Ru/NDC-8} > \text{Ru/NDC-12}$ . It is reasonably concluded that introducing more pyrrolic-N into the carbon substrates enlarges the electronic asymmetry degree of anchored Ru NCs via donating more electrons from interface Ru atoms to pyrrolic-N sites, leading to the various electronic configuration on Ru NCs to accelerate the individual reaction steps involved in alkaline HER process.

In situ Fourier transform infrared spectroscopy (FT-IR) technology was conducted to monitor bonding states of absorbed  $\text{H}_2\text{O}$  with HER

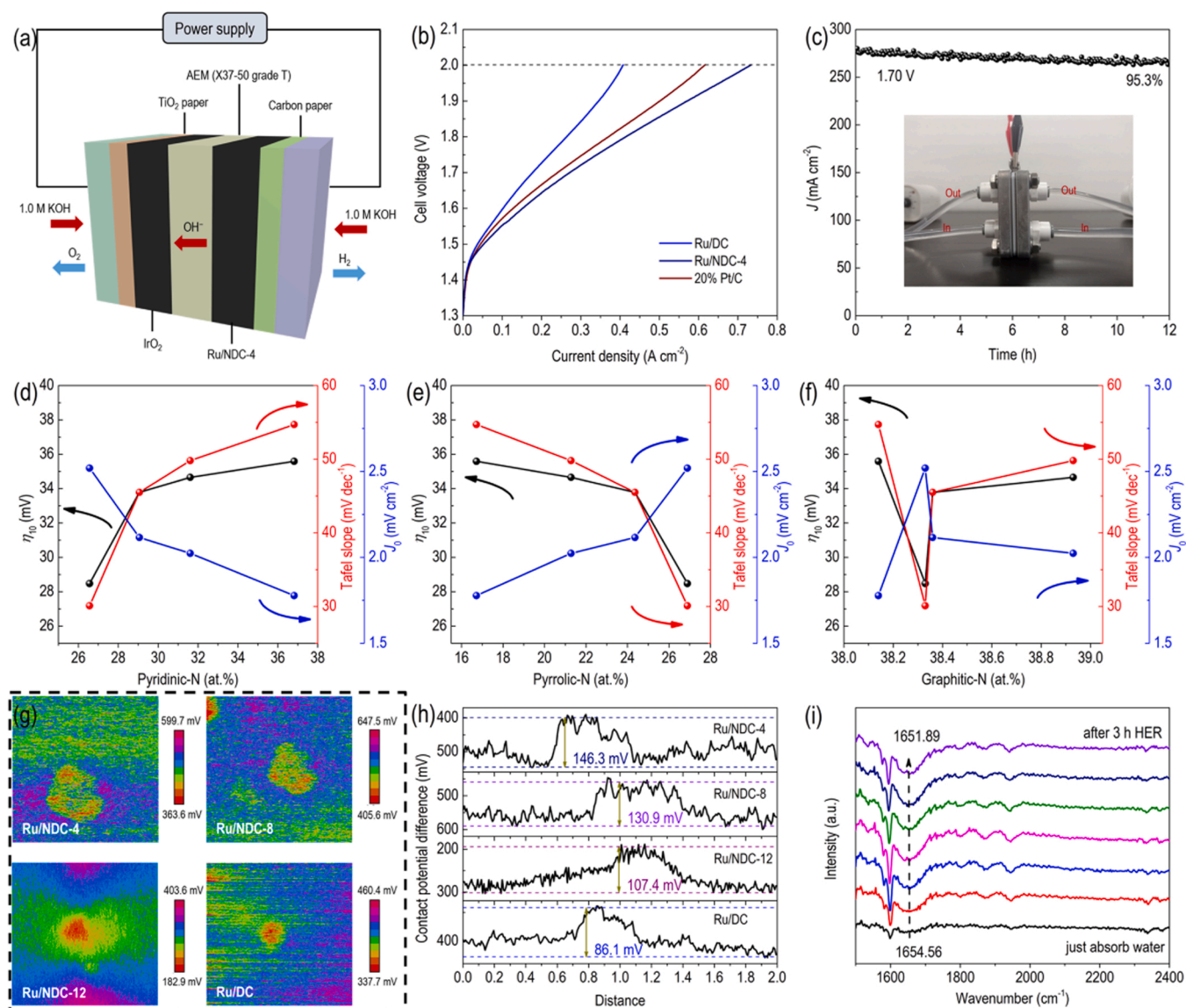


**Fig. 4.** (a) Schematic diagram of an AEM electrolyzer. (b) AEMWE polarization curves for different cathode catalysts. (c) Chronoamperometry curve of Ru/NDC-4-based AEMWE cell under static potential of 1.70 V. The inset shows photographs of the AEM electrolyzer. Dependence of overpotentials at the cathodic current density of 10 mA cm<sup>-2</sup>, Tafel slopes, and  $J_0$  on the content of pyridinic N (d), pyrrolic-N (e), and graphitic N (f) for Ru/NDC-x. (g) Surface potential maps of Ru/NDC-4/8/12 and Ru/DC measured using Kelvin probe atomic force microscopy and (h) their corresponding potential amplitude. (i) In situ FT-IR spectrum of Ru/NDC-4 after experiencing different time during HER at the time interval of 0.5 h.

process. When just putting the Ru/NDC-4 into 1.0 M KOH to completely soak, the bending vibration peak of HO–H bond emerges at 1654.56 cm<sup>-1</sup>. As HER proceeds, the peaks on Ru/NDC-4 (Fig. 4i) exhibits the red-shift tendency from 1654.56 to 1651.89 cm<sup>-1</sup>, demonstrating HO–H bonds become weaker with the progression of HER [41, 49]. In contrast, Ru/DC displays almost negligible shift of those peaks within 3 h HER test (Fig. S34). All of the outcomes unquestionably demonstrate that the asymmetrical electronic distribution on Ru NCs originated from the synergistic action of N functional groups and Ru NCs evidently promote the decomposition of surface H<sub>2</sub>O. The facile breaking down of HO–H bond would supply more H\* for the following Tafel step, thereby accelerating the overall reaction kinetics of Ru/NDC-4 toward alkaline HER, which is consistent with Tafel slope investigations [50].

The excellent electrocatalytic activities of Ru/NDC-4 inspire us to explore the underlying mechanism. With respect to alkaline HER process, it involves the multiple reaction steps and intermediates, therefore, at least two types of active sites are required to break the scaling relation

for the adsorption behaviors of various intermediates [19]. Interestingly, as reflected by the spectroscopy characterizations and the stimulated distribution of charge density, the significant electronic asymmetry of Ru/NDC creates at least three possible active sites, namely, electron accumulated NDC substrate, positively charged near-interface Ru sites, and non-interfacial Ru atoms with higher electron density, to take part in the alkaline HER. To better understand the effect of surface electron asymmetric degree on electrocatalytic performance, the density functional theory (DFT) calculations were conducted.

On the basis of the experiment results and Bader charge analysis, we know that the pyrrolic-N dominated carbon substrates induce more extraordinary electron asymmetric degree of Ru NCs and superior HER performance. Herein, to simply the calculation system, the pyrrolic-N doped graphene was first applied to simulate NDC. As for Ru/NDC catalyst, there exists three possible active sites involved in HER process, namely, electron accumulated NDC substrate of Ru/NDC (labeled as accu-NDC), near-interface Ru site of Ru/NDC (labeled as near-Ru<sub>55</sub>/



NDC), and non-interfacial Ru atom of Ru/NDC (labeled as non-Ru<sub>55</sub>/NDC). Therefore, the interaction between all possible active sites and reactants/intermediates involved in HER were calculated. The corresponding optimized configuration were exhibited in Figs. S35–S37. Specially, since H<sub>2</sub>O adsorption is the first step of alkaline HER, the interaction behavior of H<sub>2</sub>O on the possible catalytic sites was first calculated [51]. The calculated H<sub>2</sub>O-adsorption Gibbs free energy ( $\Delta G_{\text{H}_2\text{O}}$ ) is estimated to be  $-0.68$ ,  $-0.27$ ,  $-1.06$ , and  $-0.96$  eV for Ru<sub>55</sub> cluster, accu-NDC, near-Ru<sub>55</sub>/NDC, and non-Ru<sub>55</sub>/NDC (Fig. 5a), respectively, indicating that the electron deficient Ru atoms at the interface promote nucleophilic attack from H<sub>2</sub>O and subsequently

accelerate the cleavage of HO–H bond to achieve fast proton supply. Additionally, the energy barrier for water dissociation was also measured to investigate the rate-determining step of catalysts in alkaline electrolyte. Due to the poor H<sub>2</sub>O adsorption ability, the subsequent water dissociation step is hardly occurred on the electron accumulated NDC substrate of Ru/NDC. The energy barrier for water dissociation is calculated to be  $-0.85$ ,  $-0.18$ , and  $-1.03$  eV for Ru<sub>55</sub> cluster, near-Ru<sub>55</sub>/NDC, and non-Ru<sub>55</sub>/NDC (Fig. 5b), respectively, implying that the water dissociation mostly takes place at the interface in Ru-NDC heterointerfaces.

Usually, the intrinsic HER performance of electrocatalysts was

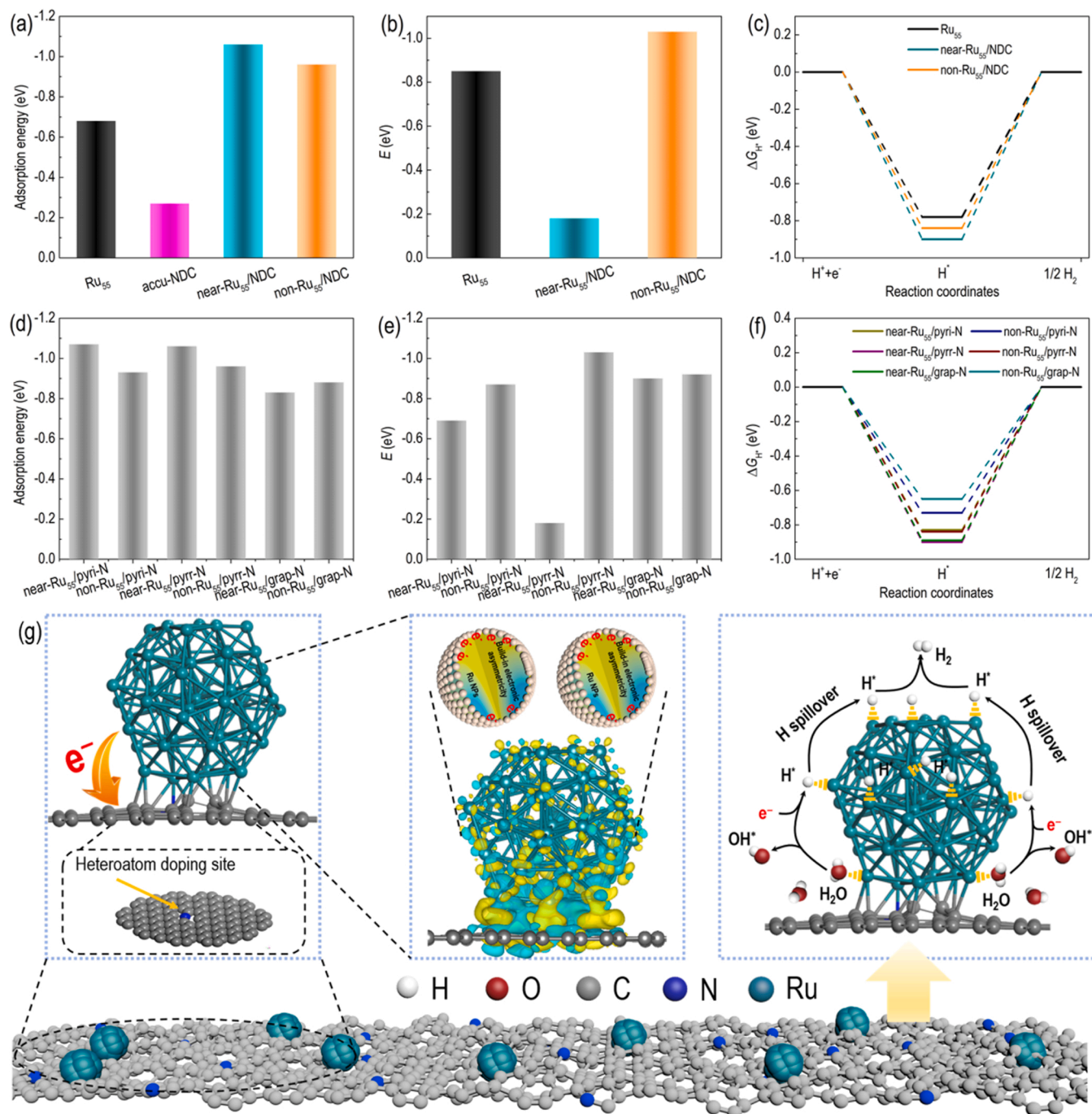


**Fig. 5.** DFT-simulated adsorption behavior of reactants and intermediates. (a) H<sub>2</sub>O adsorption energy on Ru<sub>55</sub> cluster, accu-NDC, near-Ru<sub>55</sub>/NDC, and non-Ru<sub>55</sub>/NDC. (b) Energy barrier for water dissociation ( $E$ ), and (c) Gibbs free energy diagram for hydrogen adsorption ( $\Delta G_{\text{H}^+}$ ) on Ru<sub>55</sub> cluster, near-Ru<sub>55</sub>/NDC, and non-Ru<sub>55</sub>/NDC. (d) Calculated adsorption energy of H<sub>2</sub>O, (e) H<sub>2</sub>O dissociation energy barrier, and (f) Gibbs free energy diagram for hydrogen adsorption on the model structure of Ru<sub>55</sub>/NDC with different N type on graphene. (g) Schematic illustration of mechanism of the enhanced HER activity on Ru/NDC.

always investigated by the Gibbs free energy of hydrogen ( $\Delta G_{H^*}$ ) adsorption. The highest HER activity requires the value of  $\Delta G_{H^*}$  close to zero, and the closer  $\Delta G_{H^*}$  value to zero could induce more facile hydrogen adsorption and desorption. Hence, the possible reaction sites were evaluated to compare their  $\Delta G_{H^*}$  value. The calculated results in Fig. 5c exhibit that the  $\Delta G_{H^*}$  value of Ru/NDC on the surface Ru atom ( $-0.84$  eV) is positive than the interfacial Ru site ( $-0.90$  eV), implying that the electron-enriched Ru atoms at the surface are helpful for  $H^*$  adsorption. Specially, benefiting from the great hydrogen affinity of the electron-enriched Ru species, the migration of hydrogen obtained from HO–H cleavage from the interfacial Ru atoms to the surface Ru sites would easily happen via hydrogen spillover [52,53]. Therefore, all the theoretical calculations demonstrate that the electron asymmetry in Ru/NDC heterostructures contributes to attain a sufficient binding affinity for water adsorption and dissociation at interfacial Ru sites and adsorb electron-deficient  $H^*$  on the negatively charged Ru atoms in surface, which together finish the steps involved in alkaline HER and result in the evidently improved HER activity.

Meanwhile, to further consolidate our assumption about pyrrolic-N dominated electron effect on alkaline HER performance, the interaction between Ru<sub>55</sub>/NDC with pyridinic-N/graphitic-N and reactants/intermediates involved in HER were further calculated. The corresponding optimized configuration were presented in Figs. S38–S40 and the relevant free energy diagrams were plotted in Fig. 5d–f. All relevant results indicate that the near-interface Ru sites are favorable for water adsorption and dissociation, while the non-interfacial Ru atoms are helpful for hydrogen adsorption. Moreover, the calculated results also demonstrate that Ru<sub>55</sub>/pyrrolic-N doped graphene model has the more favorable adsorption behaviors compared to other structures, which is consistent with their activity measurements toward HER. Therefore, the balance between H<sub>2</sub>O adsorption/dissociation and the optimized hydrogen adsorption on the two regions of Ru NCs in Ru/NDC synergistically expedites the Volmer–Tafel steps involved in alkaline HER and results in the evidently improved HER activity. Hence, the proposed alkaline HER mechanism occurred on the Ru/NDC catalyst is schematically illustrated in Fig. 5g. The electron accumulation effect of N dopants, specially pyrrolic N, on carbon substrates leads to the significant asymmetric electronic distribution on Ru NCs. The electron deficient interfacial Ru sites at heterointerfaces promote water cleavage to produce H atoms and OH<sup>−</sup> species. And then, the H atoms move to the adjacent Ru sites and convert into the adsorbed  $H^*$  intermediates. Subsequently, the  $H^*$  will migrate from the interfacial Ru sites to the electron-enriched non-interfacial Ru atoms via hydrogen spillover. Finally, the migrated  $H^*$  on the surface Ru sites would combine into H<sub>2</sub> molecules, which escape from Ru NCs surface and finish HER process.

#### 4. Conclusions

In conclusion, we have designed Ru/NDC heterostructures in which ultrafine Ru NCs were anchored on nitrogen-doped carbon substrates with controllable electronic asymmetry of Ru sites. Specially, the pyrrolic-N dominated NDC triggers largest electron migration from Ru NCs to N-doped NDC, thus giving rise to the evident electron redistribution on Ru NCs and adjusting the electronic asymmetry degree of Ru NCs. As a result, the optimized Ru/NDC catalyst shows outstanding HER and remarkable AEMWE single-cell performance in alkaline media. This work proves and manifests the significance of electronic asymmetry on the performance of electrocatalysts from the investigation of experiments and theoretical simulations. We envisage that this brilliant attempt would provide in-depth understanding of the electronic asymmetry of active species and further guides the reasonable design of the highly active and robust catalysts for various electrochemical and catalytic applications.

#### CRediT authorship contribution statement

**Jin-Tao Ren:** Conceptualization, Methodology, Investigation, Writing – original draft, Funding acquisition. **Lei Chen:** Investigation, Software, Writing – review & editing. **Hao-Yu Wang:** Formal analysis, Writing – review & editing. **Wen-Wen Tian:** Formal analysis, Writing – review & editing. **Xu Zhang:** DFT calculation, Writing – review & editing. **Tian-Yi Ma:** Conceptualization, Resources, Writing – review & editing. **Zheng Zhou:** Resources, Writing – review & editing. **Zhong-Yong Yuan:** Supervision, Funding acquisition, Project administration.

#### Declaration of Competing Interest

The authors declare that they have no known competing financial interests or personal relationships that could have appeared to influence the work reported in this paper.

#### Data availability

Data will be made available on request.

#### Acknowledgments

This work was supported by the National Natural Science Foundation of China (22179065, 22105108, and 22111530112), China Postdoctoral Science Foundation (2020M680860), and the Smart Sensing Interdisciplinary Science Center, Nankai University.

#### Appendix A. Supplementary material

Supplementary data associated with this article can be found in the online version at doi:10.1016/j.apcatb.2023.122466.

#### References

- [1] J. Wang, W. Cui, Q. Liu, Z. Xing, A.M. Asiri, X. Sun, Recent progress in cobalt-based heterogeneous catalysts for electrochemical water splitting, *Adv. Mater.* 28 (2016) 215–230, <https://doi.org/10.1002/adma.201502696>.
- [2] J. Wang, F. Xu, H. Jin, Y. Chen, Y. Wang, Non-noble metal-based carbon composites in hydrogen evolution reaction: fundamentals to applications, *Adv. Mater.* 29 (2017) 1605838, <https://doi.org/10.1002/adma.201605838>.
- [3] T. Liu, W. Zhang, T. Chen, D. Liu, L. Cao, T. Ding, X. Liu, B. Pang, S. Wang, L. Wang, Q. Luo, T. Yao, Regulating the coordination environment of ruthenium cluster catalysts for the alkaline hydrogen evolution reaction, *J. Phys. Chem. Lett.* 12 (2021) 8016–8023, <https://doi.org/10.1021/acs.jpclett.1c01936>.
- [4] P. Zhu, X. Xiong, D. Wang, Regulations of active moiety in single atom catalysts for electrochemical hydrogen evolution reaction, *Nano Res.* 15 (2022) 5792–5815, <https://doi.org/10.1007/s12274-022-4265-y>.
- [5] Q. Dai, L. Wang, K. Wang, X. Sang, Z. Li, B. Yang, J. Chen, L. Lei, L. Dai, Y. Hou, Accelerated water dissociation kinetics by electron-enriched cobalt sites for efficient alkaline hydrogen evolution, *Adv. Funct. Mater.* 32 (2022) 2109556, <https://doi.org/10.1002/adfm.202109556>.
- [6] D. Chen, R. Lu, R. Yu, Y. Dai, H. Zhao, D. Wu, P. Wang, J. Zhu, Z. Pu, L. Chen, J. Yu, S. Mu, Work-function-induced interfacial built-in electric fields in Os–OsSe<sub>2</sub> heterostructures for active acidic and alkaline hydrogen evolution, *Angew. Chem. Int. Ed.* 61 (2022), e202208642, <https://doi.org/10.1002/anie.202208642>.
- [7] Y. He, X. Zhuang, C. Lei, L. Lei, Y. Hou, Y. Mai, X. Feng, Porous carbon nanosheets: synthetic strategies and electrochemical energy related applications, *Nano Today* 24 (2019) 103–119, <https://doi.org/10.1016/j.nantod.2018.12.004>.
- [8] K. Yuan, C. Lu, S. Sfaelou, X. Liao, X. Zhuang, Y. Chen, U. Scherf, X. Feng, In situ nanoarchitecture and active-site engineering toward highly efficient carbonaceous electrocatalysts, *Nano Energy* 59 (2019) 207–215, <https://doi.org/10.1016/j.nanoen.2019.02.043>.
- [9] K.-H. Wu, Y. Liu, X. Tan, Y. Liu, Y. Lin, X. Huang, Y. Ding, B.-J. Su, B. Zhang, J.-M. Chen, W. Yan, S.C. Smith, I.R. Gentle, S. Zhao, Regulating electron transfer over asymmetric low-spin Co(II) for highly selective electrocatalysis, *Chem. Catal.* 2 (2022) 372–385, <https://doi.org/10.1016/j.checat.2021.12.005>.
- [10] X. Li, H. Liu, Z. Chen, Q. Wu, Z. Yu, M. Yang, X. Wang, Z. Cheng, Z. Fu, Y. Lu, Enhancing oxygen evolution efficiency of multiferroic oxides by spintronic and ferroelectric polarization regulation, *Nat. Commun.* 10 (2019) 1409, <https://doi.org/10.1038/s41467-019-09191-0>.
- [11] C. Hu, S. Tu, N. Tian, T. Ma, Y. Zhang, H. Huang, Photocatalysis enhanced by external fields, *Angew. Chem. Int. Ed.* 60 (2021) 16309–16328, <https://doi.org/10.1002/anie.202009518>.

- [12] S. Tu, Y. Guo, Y. Zhang, C. Hu, T. Zhang, T. Ma, H. Huang, Piezocatalysis and piezo-photocatalysis: catalysts classification and modification strategy, reaction mechanism, and practical application, *Adv. Funct. Mater.* 30 (2020) 2005158, <https://doi.org/10.1002/adfm.202005158>.
- [13] X. Zhang, A. Chen, L. Chen, Z. Zhou, 2D materials bridging experiments and computations for electro/photocatalysis, *Adv. Energy Mater.* 12 (2022) 2003841, <https://doi.org/10.1002/aenm.202003841>.
- [14] L. Chen, J.T. Ren, Z.Y. Yuan, Design strategies of phosphorus-containing catalysts for photocatalytic, photoelectrochemical and electrocatalytic water splitting, *Green Chem.* 24 (2022) 713–747, <https://doi.org/10.1039/d1gc03768d>.
- [15] Y. Zheng, Y. Jiao, Y. Zhu, L.H. Li, Y. Han, Y. Chen, M. Jaroniec, S.Z. Qiao, High electrocatalytic hydrogen evolution activity of an anomalous ruthenium catalyst, *J. Am. Chem. Soc.* 138 (2016) 16174–16181, <https://doi.org/10.1021/jacs.6b11291>.
- [16] Z. Jiang, S. Song, X. Zheng, X. Liang, Z. Li, H. Gu, Z. Li, Y. Wang, S. Liu, W. Chen, D. Wang, Y. Li, Lattice strain and Schottky junction dual regulation boosts ultrafine ruthenium nanoparticles anchored on a N-modified carbon catalyst for H<sub>2</sub> production, *J. Am. Chem. Soc.* 144 (2022) 19619–19626, <https://doi.org/10.1021/jacs.2c09613>.
- [17] J. Zhu, Y. Guo, F. Liu, H. Xu, L. Gong, W. Shi, D. Chen, P. Wang, Y. Yang, C. Zhang, J. Wu, J. Luo, S. Mu, Regulative electronic states around ruthenium/ruthenium disulfide heterointerfaces for efficient water splitting in acidic media, *Angew. Chem. Int. Ed.* 60 (2021) 12328–12334, <https://doi.org/10.1002/anie.202101539>.
- [18] J. Xu, T. Liu, J. Li, B. Li, Y. Liu, B. Zhang, D. Xiong, I. Amorim, W. Li, L. Liu, Boosting the hydrogen evolution performance of ruthenium clusters through synergistic coupling with cobalt phosphide, *Energy Environ. Sci.* 11 (2018) 1819–1827, <https://doi.org/10.1039/c7ee03603e>.
- [19] Q. He, Y. Zhou, H. Shou, X. Wang, P. Zhang, W. Xu, S. Qiao, C. Wu, H. Liu, D. Liu, S. Chen, R. Long, Z. Qi, X. Wu, L. Song, Synergistic reaction kinetics over adjacent ruthenium sites for superb hydrogen generation in alkaline media, *Adv. Mater.* 34 (2022) 2110604, <https://doi.org/10.1002/adma.202110604>.
- [20] L. Li, S. Liu, C. Zhan, Y. Wen, Z. Sun, J. Han, T.-S. Chan, Q. Zhang, Z. Hu, X. Huang, Surface and lattice engineered ruthenium superstructures towards high-performance bifunctional hydrogen catalysis, *Energy Environ. Sci.* (2022), <https://doi.org/10.1039/d2ee02076a>.
- [21] S. Zhou, H. Jang, Q. Qin, L. Hou, M.G. Kim, S. Liu, X. Liu, J. Cho, Boosting hydrogen evolution reaction by phase engineering and phosphorus doping on Ru/P-TiO<sub>2</sub>, *Angew. Chem. Int. Ed.* 61 (2022), e202212196, <https://doi.org/10.1002/anie.202212196>.
- [22] Z. Liu, Y. Du, R. Yu, M. Zheng, R. Hu, J. Wu, Y. Xia, Z. Zhuang, D. Wang, Tuning mass transport in electrocatalysis down to sub-5nm through nanoscale grade separation, *Angew. Chem. Int. Ed.* 62 (2023), e202212653, <https://doi.org/10.1002/anie.202212653>.
- [23] L. Li, C. Tang, Y. Zheng, B. Xia, X. Zhou, H. Xu, S.Z. Qiao, Tailoring selectivity of electrochemical hydrogen peroxide generation by tunable pyrrolic-nitrogen-carbon, *Adv. Energy Mater.* 10 (2020) 2000789, <https://doi.org/10.1002/aenm.202000789>.
- [24] M. He, S. Song, P. Wang, Z. Fang, W. Wang, X. Yuan, C. Li, H. Li, W. Song, D. Luo, Z. Li, Carbon doped cobalt nanoparticles stabilized by carbon shell for highly efficient and stable oxygen reduction reaction, *Carbon* 196 (2022) 483–492, <https://doi.org/10.1016/j.carbon.2022.05.019>.
- [25] M. Lao, G. Zhao, P. Li, T. Ma, Y. Jiang, H. Pan, S.X. Dou, W. Sun, Manipulating the coordination chemistry of Ru-N(O)-C moieties for fast alkaline hydrogen evolution kinetics, *Adv. Funct. Mater.* 31 (2021) 2100698, <https://doi.org/10.1002/adfm.202100698>.
- [26] J. Zhang, P. Liu, G. Wang, P.P. Zhang, X.D. Zhuang, M.W. Chen, I.M. Weidinger, X. L. Feng, Ruthenium/nitrogen-doped carbon as an electrocatalyst for efficient hydrogen evolution in alkaline solution, *J. Mater. Chem. A* 5 (2017) 25314–25318, <https://doi.org/10.1039/c7ta08764k>.
- [27] B. Lu, L. Guo, F. Wu, Y. Peng, J.E. Lu, T.J. Smart, N. Wang, Y.Z. Finck, D. Morris, P. Zhang, N. Li, P. Gao, Y. Ping, S. Chen, Ruthenium atomically dispersed in carbon outperforms platinum toward hydrogen evolution in alkaline media, *Nat. Commun.* 10 (2019) 631, <https://doi.org/10.1038/s41467-019-08419-3>.
- [28] J.T. Ren, Z.Y. Yuan, A universal route to N-coordinated metals anchored on porous carbon nanosheets for highly efficient oxygen electrochemistry, *J. Mater. Chem. A* 7 (2019) 13591–13601, <https://doi.org/10.1039/c9ta03300a>.
- [29] W. Zhang, W. Chen, Q. Xiao, L. Yu, C. Huang, G. Lu, A.W. Morawski, Y. Yu, Nitrogen-coordinated metallic cobalt disulfide self-encapsulated in graphitic carbon for electrochemical water oxidation, *Appl. Catal. B* 268 (2020), 118449, <https://doi.org/10.1016/j.apcatb.2019.118449>.
- [30] X.W. Lv, X.L. Liu, Y.J. Suo, Y.P. Liu, Z.Y. Yuan, Identifying the dominant role of pyridinic-N-Mo bonding in synergistic electrocatalysis for ambient nitrogen reduction, *ACS Nano* 15 (2021) 12109–12118, <https://doi.org/10.1021/acsnano.1c03465>.
- [31] Y. Guo, P. Yuan, J. Zhang, H. Xia, F. Cheng, M. Zhou, J. Li, Y. Qiao, S. Mu, Q. Xu, Co<sub>2</sub>P-CoN double active centers confined in N-doped carbon nanotube: heterostructural engineering for trifunctional catalysis toward HER, ORR, OER, and Zn-air batteries driven water splitting, *Adv. Funct. Mater.* 28 (2018) 1805641, <https://doi.org/10.1002/adfm.201805641>.
- [32] G. Lin, Q. Ju, Y. Jin, X. Qi, W. Liu, F. Huang, J. Wang, Suppressing dissolution of Pt-based electrocatalysts through the electronic metal-support interaction, *Adv. Energy Mater.* 11 (2021) 2101050, <https://doi.org/10.1002/aenm.202101050>.
- [33] Z. Huang, Q. Zhou, J. Wang, Y. Yu, Fermi-level-tuned MOF-derived N-ZnO@NC for photocatalysis: A key role of pyridine-N-Zn bond, *J. Mater. Sci. Technol.* 112 (2022) 68–76, <https://doi.org/10.1016/j.jmst.2021.10.017>.
- [34] H. Li, X. Wu, P. Wang, S. Song, M. He, C. Li, W. Wang, Z. Fang, X. Yuan, W. Song, Z. Li, Interface engineering of hollow CoO/Co<sub>4</sub>S<sub>3</sub>@CoO/Co<sub>4</sub>S<sub>3</sub> heterojunction for highly stable and efficient electrocatalytic overall water splitting, *ACS Sustain. Chem. Eng.* 10 (2022) 13112–13124, <https://doi.org/10.1021/acssuschemeng.2c03609>.
- [35] X. Gu, M. Yu, S. Chen, X. Mu, Z. Xu, W. Shao, J. Zhu, C. Chen, S. Liu, S. Mu, Coordination environment of Ru clusters with in-situ generated metastable symmetry-breaking centers for seawater electrolysis, *Nano Energy* 102 (2022), 107656, <https://doi.org/10.1016/j.nanoen.2022.107656>.
- [36] K. Tu, D. Tranca, F. Rodríguez-Hernández, K. Jiang, S. Huang, Q. Zheng, M. X. Chen, C. Lu, Y. Su, Z. Chen, H. Mao, C. Yang, J. Jiang, H.W. Liang, X. Zhuang, A novel heterostructure based on RuMo nanoalloys and N-doped carbon as an efficient electrocatalyst for the hydrogen evolution reaction, *Adv. Mater.* 32 (2020) 2005433, <https://doi.org/10.1002/adma.202005433>.
- [37] J. Luo, J. Wang, Y. Guo, J. Zhu, H. Jin, Z. Zhang, D. Zhang, Y. Niu, S. Hou, J. Du, D. He, Y. Xiong, L. Chen, S. Mu, Y. Huang, Metal-organic frameworks derived RuP<sub>2</sub> with yolk-shell structure and efficient performance for hydrogen evolution reaction in both acidic and alkaline media, *Appl. Catal. B* 305 (2022), 121043, <https://doi.org/10.1016/j.apcatb.2021.121043>.
- [38] W. Yu, H. Huang, Y. Qin, D. Zhang, Y. Zhang, K. Liu, Y. Zhang, J. Lai, L. Wang, The synergistic effect of pyrrolic-N and pyridinic-N with Pt under strong metal-support interaction to achieve high-performance alkaline hydrogen evolution, *Adv. Energy Mater.* 12 (2022) 2200110, <https://doi.org/10.1002/aenm.202200110>.
- [39] Z. Li, C. Yu, Y. Wen, Y. Gao, X. Xing, Z. Wei, H. Sun, Y.-W. Zhang, W. Song, Mesoporous hollow Cu–Ni alloy nanocage from core-shell Cu@Ni nanocube for efficient hydrogen evolution reaction, *ACS Catal.* 9 (2019) 5084–5095, <https://doi.org/10.1021/acscatal.8b04814>.
- [40] Y. Pei, S. Guo, Q. Ju, Z. Li, P. Zhuang, R. Ma, Y. Hu, Y. Zhu, M. Yang, Y. Zhou, J. Shen, J. Wang, Interface engineering with ultralow ruthenium loading for efficient water splitting, *ACS Appl. Mater. Interfaces* 12 (2020) 36177–36185, <https://doi.org/10.1021/acsaami.0c09593>.
- [41] Z. Dong, F. Lin, Y. Yao, L. Jiao, Crystalline Ni(OH)<sub>2</sub>/amorphous NiMoO<sub>4</sub> mixed-catalyst with Pt-like performance for hydrogen production, *Adv. Energy Mater.* 9 (2019) 1902703, <https://doi.org/10.1002/aenm.201902703>.
- [42] J. Mahmood, F. Li, S.M. Jung, M.S. Okyay, I. Ahmad, S.J. Kim, N. Park, H.Y. Jeong, J.B. Baek, An efficient and pH-universal ruthenium-based catalyst for the hydrogen evolution reaction, *Nat. Nanotechnol.* 12 (2017) 441–446, <https://doi.org/10.1038/nnano.2016.304>.
- [43] D.S. Baek, G.Y. Jung, B. Seo, J.C. Kim, H.W. Lee, T.J. Shin, H.Y. Jeong, S.K. Kwak, S.H. Jo, Ordered mesoporous metastable α-MoC<sub>1-x</sub> with enhanced water dissociation capability for boosting alkaline hydrogen evolution activity, *Adv. Funct. Mater.* 29 (2019) 1901217, <https://doi.org/10.1002/adfm.201901217>.
- [44] Y. Zhu, P. Tian, H. Jiang, J. Mu, L. Meng, X. Su, Y. Wang, Y. Lin, Y. Zhu, L. Song, C. Li, Synergistic effect of platinum single atoms and nanoclusters boosting electrocatalytic hydrogen evolution, *CCS Chem.* 3 (2021) 2539–2547, <https://doi.org/10.31635/ccschem.020.202000497>.
- [45] G. Li, P. Wang, C. Li, Z. Fang, M. He, W. Wang, X. Yuan, H. Li, P. Li, Z. Li, Cobalt-nickel layered double hydroxide on hollow Co<sub>3</sub>S<sub>4</sub>/CuS derived from ZIF-67 for efficient overall water splitting, *Mater. Res. Lett.* 10 (2022) 744–753, <https://doi.org/10.1080/21663831.2022.2095235>.
- [46] X. Jiang, H. Jang, S. Liu, Z. Li, M.G. Kim, C. Li, Q. Qin, X. Liu, J. Cho, The heterostructure of Ru<sub>2</sub>P/WO<sub>3</sub>/NPC synergistically promotes H<sub>2</sub>O dissociation for improved hydrogen evolution, *Angew. Chem. Int. Ed.* 60 (2021) 4110–4116, <https://doi.org/10.1002/anie.202014411>.
- [47] Z. Li, C. Yu, Y. Kang, X. Zhang, Y. Wen, Z.K. Wang, C. Ma, C. Wang, K. Wang, X. Qu, M. He, Y.W. Zhang, W. Song, Ultra-small hollow ternary alloy nanoparticles for efficient hydrogen evolution reaction, *Natl. Sci. Rev.* 8 (2020) nwa204, <https://doi.org/10.1093/nsr/nwaa204>.
- [48] B. Lin, J. Chen, R. Yang, S. Mao, M. Qin, Y. Wang, Multi-hierarchical cobalt-based electrocatalyst towards high rate H<sub>2</sub> production, *Appl. Catal. B* 316 (2022), 121666, <https://doi.org/10.1016/j.apcatb.2022.121666>.
- [49] L. Yang, L. Huang, Y. Yao, L. Jiao, In-situ construction of lattice-matching NiP<sub>2</sub>/NiSe<sub>2</sub> heterointerfaces with electron redistribution for boosting overall water splitting, *Appl. Catal. B* 282 (2021), 119584, <https://doi.org/10.1016/j.apcatb.2020.119584>.
- [50] D. Xue, J. Cheng, P. Yuan, B.A. Lu, H. Xia, C.C. Yang, C.L. Dong, H. Zhang, F. Shi, S. C. Mu, J.S. Hu, S.G. Sun, J.N. Zhang, Boron-tethering and regulative electronic states around iridium species for hydrogen evolution, *Adv. Funct. Mater.* 32 (2022) 2113191, <https://doi.org/10.1002/adfm.202113191>.
- [51] G. Chen, T. Wang, J. Zhang, P. Liu, H. Sun, X. Zhuang, M. Chen, X. Feng, Accelerated hydrogen evolution kinetics on NiFe-layered double hydroxide electrocatalysts by tailoring water dissociation active sites, *Adv. Mater.* 30 (2018) 1706279, <https://doi.org/10.1002/adma.201706279>.
- [52] J. Park, S. Lee, H.E. Kim, A. Cho, S. Kim, Y. Ye, J.W. Han, H. Lee, J.H. Jang, J. Lee, Investigation of the support effect in atomically dispersed Pt on WO<sub>3-x</sub> for utilization of Pt in the hydrogen evolution reaction, *Angew. Chem. Int. Ed.* 58 (2019) 16038–16042, <https://doi.org/10.1002/anie.201908122>.
- [53] J. Huang, J. Han, T. Wu, K. Feng, T. Yao, X. Wang, S. Liu, J. Zhong, Z. Zhang, Y. Zhang, B. Song, Boosting hydrogen transfer during volmer reaction at oxides/metal nanocomposites for efficient alkaline hydrogen evolution, *ACS Energy Lett.* 4 (2019) 3002–3010, <https://doi.org/10.1021/acsenylett.9b02359>.